U.S. DEPARTMENT OF ENERGY

PNNL-39775

Prepared for the U.S. Department of Energy
under Contract DE-AC05-76RL01830

Microstructural and compositional effects of individual and sequential He^+ and D_2^+ ion irradiations in γ-$LiAlO_2$ pellets

Weilin Jiang
Andrew M. Casella
David J. Senor

Final Report
Tritium Modernization Program
September 2026

Pacific Northwest
NATIONAL LABORATORY

Proudly Operated by Battelle *Since 1965*

DISCLAIMER

This information was prepared as an account of work sponsored by an agency of the U.S. Government. Neither the U.S. Government nor any agency thereof, nor any of their employees, makes any warranty, expressed or implied, or assumes any legal liability or responsibility for the accuracy, completeness, or usefulness, of any information, apparatus, product, or process disclosed, or represents that its use would not infringe privately owned rights. References herein to any specific commercial product, process, or service by trade name, trade mark, manufacturer, or otherwise, does not necessarily constitute or imply its endorsement, recommendation, or favoring by the U.S. Government or any agency thereof. The views and opinions of authors expressed herein do not necessarily state or reflect those of the U.S. Government or any agency thereof.

Microstructural and compositional effects of individual and sequential He^+ and D_2^+ ion irradiations in γ-$LiAlO_2$ pellets

Weilin Jiang, Andrew M. Casella, David J. Senor
PNNL Contributors: Libor Kovarik, Zihua Zhu, Bethany Matthews
Texas A&M University Contributors: Zhihan Hu, Lin Shao

Summary

This study, conducted from November 2025 to September 2026, investigates the individual and combined effects of He^+ and D_2^+ irradiations on the microstructural evolution, Li redistribution, and D retention in γ-$LiAlO_2$ pellets. Experiments were performed at 773 K using He^+-only, D_2^+-only, and sequential He^+ and D_2^+ irradiations in three regions of a pellet to fluences of 2×10^{17} He^+/cm^2, 2×10^{17} D^+/cm^2, and 2×10^{17} $(He^+ + D^+)/cm^2$, respectively, at an ion flux of ~1×10^{13} $(ions/cm^2)/s$. A second pellet was irradiated under the same conditions but at a lower flux of ~4×10^{12} $(ions/cm^2)/s$ for all three irradiation conditions.

The results show higher non-gas D retention following sequential He^+ and D_2^+ irradiation than following D_2^+-only irradiation at both dose rates, suggesting that He-vacancy clusters form and provide effective D trapping sites. Lower dose rate resulted in increased D retention, consistent with greater time for D diffusion and trapping at stable defects. At the high dose rate, He^+-only irradiation produced He blisters, a polycrystalline region containing nanoscale precipitates and cavities, and, tentatively, a deeper featureless crystalline region in which non-gas D remains trapped. D_2^+-only irradiation produced a crystalline surface layer with cavities, followed by a region containing large, faceted $LiAl_5O_8$-type precipitates surrounded by cavities. Preferential cavity formation was observed at grain boundaries. Sequential He^+ and D_2^+ irradiation produced an amorphous surface layer with a high density of cavities and substantial Li depletion, followed by precipitate-cavity formation. These results indicate that the sequential microstructure arises from coupled damage accumulation, amorphization, gas transport, Li redistribution, precipitation, and cavity evolution rather than a simple superposition of the individual irradiation responses. Reducing the sequential irradiation dose rate from 3.8×10^{-4} to 1.5×10^{-4} dpa/s suppressed or inhibited Li depletion, amorphization, and the formation of large blisters while preserving a crystalline surface layer. Precipitate and cavity formation, including preferential cavity accumulation at grain boundaries, remained evident. These observations indicate that lower dose rates provide greater opportunity for defect recombination, migration to sinks, and dynamic recovery.

Overall, the results establish that He^+ irradiation-induced He-vacancy clusters enhance D trapping, while irradiation dose rate controls the balance between defect accumulation and recovery and therefore governs the Li redistribution and microstructural evolution. The findings demonstrate the importance of gas–defect interactions, defect-sink behavior, and dose rate in determining the irradiation response of γ-$LiAlO_2$ pellets and provide a mechanistic basis for understanding tritium retention and microstructural evolution in neutron-irradiated γ-$LiAlO_2$ under reactor-relevant conditions.

Table of Contents

Summary i
Table of Contents ii
1. Introduction 1
2. Experimental Procedures 2
   2.1. SRIM simulation 2
   2.2. Ion irradiation 4
   2.3. Sample characterization 5
3. Results and Discussion 6
   3.1. Deuterium retention and lithium depletion 6
   3.2. Microstructural features 8
      3.2.1. He^+ irradiation 8
      3.2.2. D_2^+ irradiation 10
      3.2.3. Sequential He^+ and D_2^+ irradiation 13
      3.2.4. Microstructural comparison 16
   3.3. Low dose-rate case 18
4. Conclusions 22
5. Acknowledgments 23
6. References 23

1. Introduction

γ-$LiAlO_2$ pellets irradiated with a thermalized fission neutron spectrum at ~ 573 K exhibit several characteristic microstructural features, as shown in Fig. 1. The 2.05 MeV helium and 2.73 MeV tritium particles generated by the transmutation of ^6Li through thermal-neutron capture produce lattice damage by initiating displacement cascades. The subsequent thermal and irradiation-enhanced diffusion of point defects, together with their interactions, leads to the formation of extended defects, including precipitates and cavities. The resulting microstructure is characterized as $LiAl_5O_8$ precipitates surrounded by cavities, cavities within the matrix, preferential cavity formation along grain boundaries, and denuded zones adjacent to grain boundaries and the surface.

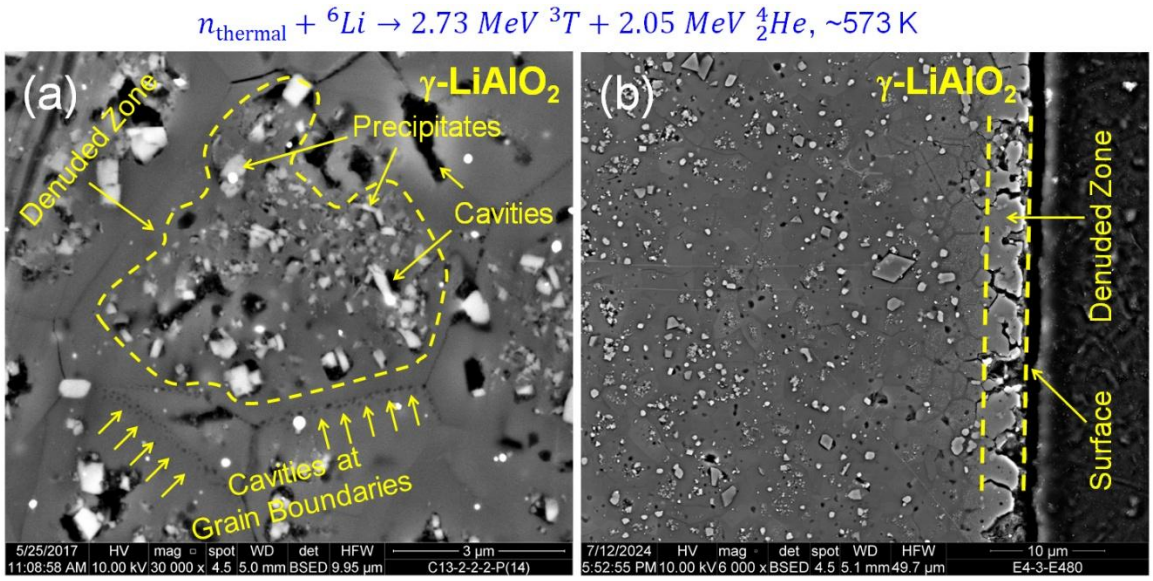


Figure 1. SEM micrographs showing the microstructure of γ-$LiAlO_2$ pellets irradiated with a thermalized fission neutron spectrum at ~573 K: (a) bulk region and (b) near-surface region.

Over the past decade, we have simulated the response of γ-$LiAlO_2$ pellets to the thermal-neutron irradiation using sequential He^+ and D_2^+ ion irradiations at elevated temperatures, with deuterium serving as a surrogate for tritium. This approach has successfully reproduced all microstructural features observed in neutron-irradiated γ-$LiAlO_2$ pellets, as shown in Fig. 2. These include the formation of non-stoichiometric $LiAl_5O_8$ precipitates surrounded by cavities [1], cavity aggregation at grain boundaries accompanied by denuded zones [2], isotopic exchange between mobile H and trapped D [3], and Li volatility [4]. More recently, we have extended these studies to investigate the effects of irradiation temperature [5] and dose-rate [6] on microstructural and compositional evolution. In contrast to low-dose-rate ion irradiation, high-dose-rate irradiation produces an amorphized surface layer, as shown in Fig. 2(b). A typical high-dose-rate-irradiated γ-$LiAlO_2$ microstructure exhibits several distinct features, including an amorphized surface layer, a fracture likely filled with gas at the crystalline–amorphous interface, followed by a layer containing precipitates surrounded by cavities [2, 7]. These features arise from the combined effects of sequential He^+ and D_2^+ irradiation, which induce complex defect production,

gas accumulation, and gas–material interactions. These observations raise several important questions: Which microstructural features can be specifically attributed to He^+ or D_2^+ irradiation? How does subsequent D_2^+ irradiation modify the pre-existing He^+-induced microstructure? And to what extent does prior He^+ irradiation influence D retention within the pellet?

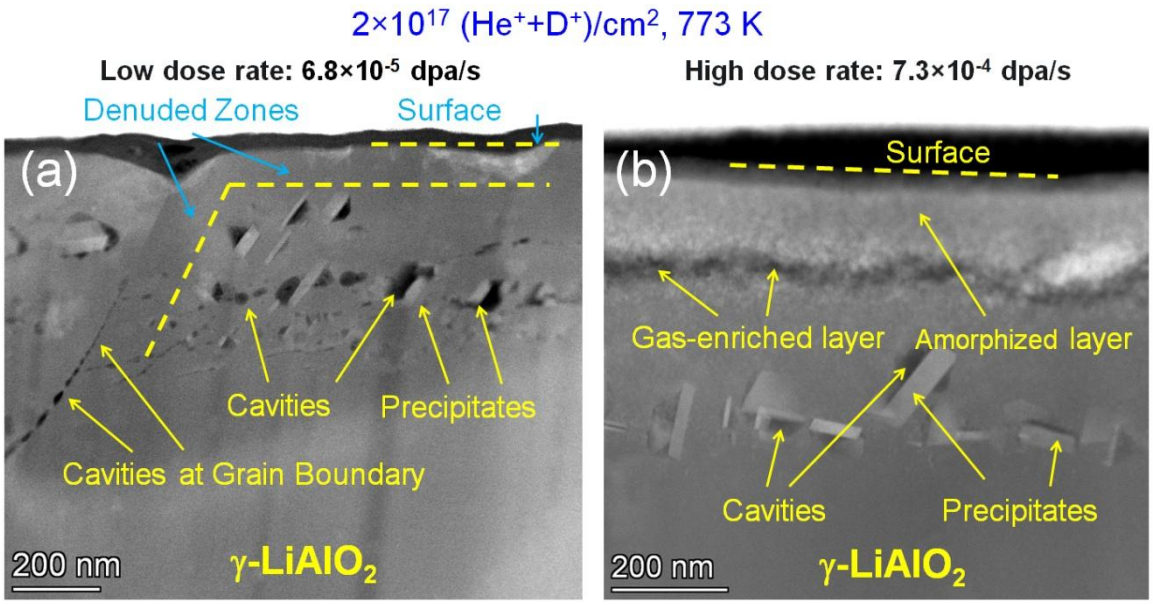


Figure 2. STEM micrographs showing the microstructures of γ-$LiAlO_2$ pellets irradiated to 2×10^{17} $(He^+ + D^+)/cm^2$ at 773 K at dose rates of (a) 7.3×10^{-4} and (b) 6.8×10^{-5} dpa/s.

To address these questions, we have performed a systematic study of both individual and sequential He^+ and D_2^+ irradiations of γ-$LiAlO_2$ pellets. The objective of this research is to isolate the contributions of each irradiation and determine how He^+-induced damage influences deuterium retention. By comparing the microstructures produced by individual versus sequential irradiations, we can directly correlate specific microstructural features with the corresponding irradiation conditions and evaluate their coupled effects on precipitation, amorphization, Li volatility, and deuterium trapping. Ultimately, this study will provide critical insights into the fundamental mechanisms governing radiation-induced microstructural evolution and tritium trapping in γ-$LiAlO_2$ under reactor-relevant conditions.

2. Experimental Procedures

2.1. SRIM simulation

To emulate the trapping of deuterium atoms, used as a surrogate for tritium, at defect sites generated by He^+ irradiation, a sequential irradiation scheme consisting of He^+ irradiation followed by D^+ irradiation was designed. The irradiation conditions were selected so that the implanted D concentration profile spatially overlaps with the damage peak region produced by He^+ irradiation. Consistent with our earlier work, SRIM13 (Stopping and Range of Ions in Matter, version 2013) simulations [8] were performed to

guide the experimental design. The simulations were carried out for 120 keV He^+ ions and 40 keV D^+ ions incident at 60° into γ-$LiAlO_2$. The calculated profiles for an ion fluence of 2×10^{17} ions/cm^2 are shown in Fig. 3 and summarized in Table 1. These irradiation conditions produce He and D concentrations comparable to those generated in γ-$^6LiAlO_2$ pellets exposed to a thermalized fission neutron spectrum at ~573 K and a total ^{6}Li burnup of ~13 at.% [9].

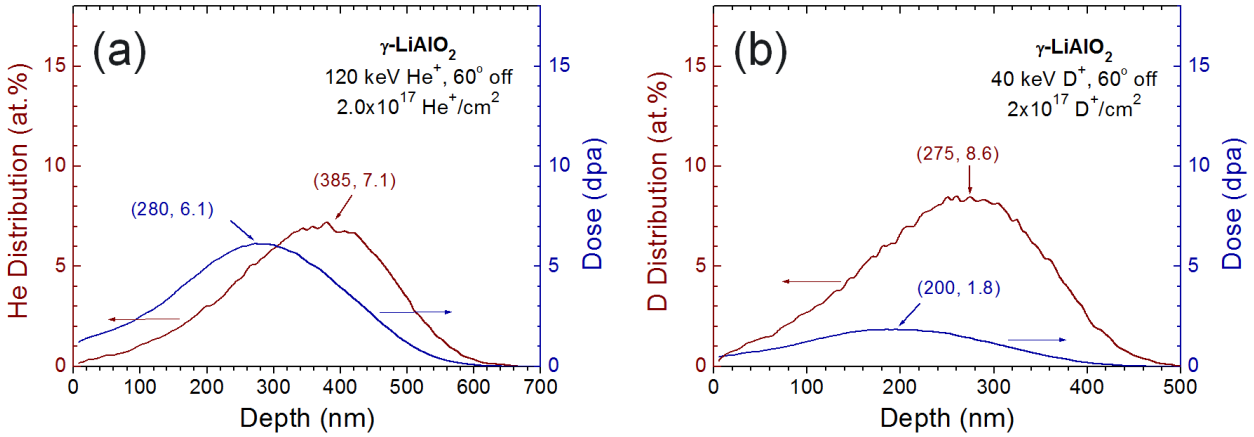


Figure 3. SRIM13-calculated depth profiles of the atomic percentages and doses for γ-$LiAlO_2$ irradiated with (a) 120 keV He^+ and (b) 40 keV D^+ ions at an incidence angle of 60° from the surface normal to a fluence of 2×10^{17} ions/cm^2.

Table 1. SRIM13 simulation results and dose rates for ion irradiation of γ-$LiAlO_2$ at 773 K to a fluence of 2×10^{17} He^+ or D^+/cm^2 at 60° off surface normal.

Ion Beam	Ion Flux (ions/cm^2/s)	Damage Peak (nm)	Dose (dpa)	Dose Rate (dpa/s)	Concentration Peak (nm)	Concentration (at.% He or D)
120 keV He^+	1×10^{13}	280	6.1	3.1×10^{-4}	385	7.1
40 keV D^+		200	1.8	9.1×10^{-5}	275	8.6
120 keV He^+	4×10^{12}	280	6.1	1.2×10^{-4}	385	7.1
40 keV D^+		200	1.8	3.6×10^{-5}	275	8.6

The combined dose rates for sequential irradiation to a total fluence of 2×10^{17} (He^++D^+)/cm^2 were 3.8×10^{-4} and 1.5×10^{-4} dpa/s at 255 nm.

To minimize artificial surface damage effects from energetic light-ion irradiation, the "monolayer collision step/surface sputtering" option in SRIM13 was employed. The threshold displacement energies were set to E_d(Li) = 22 eV, E_d(Al) = 84 eV, and E_d(O) = 37 eV, based on molecular dynamics (MD) simulations [10]. The surface binding energy for each sublattice was set equal to its corresponding threshold displacement energy. The resulting SRIM13 predictions for the peak displacements per atom (dpa) and maximum implanted-ion concentrations are summarized in Table 1. For He^+ ion irradiation, the peak dose reaches 6.1 dpa at a depth of ~280 nm, while the He concentration reaches a maximum of 7.1

at.% at ~385 nm. For D^+ ion irradiation, the peak dose is 1.8 dpa at ~200 nm, with a peak D concentration of 8.6 at.% at ~275 nm. The maximum combined dose from both irradiations is 7.55 dpa at ~255 nm. As intended, the implanted D profile is well aligned with the region of He^+ ion irradiation-induced damage. This spatial overlap ensures that D atoms are introduced into regions containing a high density of pre-existing He^+-induced defects, thereby enabling effective emulation of tritium trapping at He^+ ion-irradiation-induced defect structures in γ-$LiAlO_2$.

2.2. Ion irradiation

Ion irradiation experiments were conducted using a 140 kV ion accelerator equipped with a magnetic beam-rastering system at Texas A&M University. The γ-$LiAlO_2$ and $LiAl_5O_8$ pellets were first irradiated with 120 keV He^+ ions while a mask covered the lower portion of each pellet. This was followed by irradiation with 80 keV D_2^+ ions, equivalent to 40 keV D^+ ions, while a mask covered the upper portion of the pellets. This masking scheme produced three distinct irradiation regions: He^+-only, sequential He^++D_2^+, and D_2^+-only, as illustrated schematically in Fig. 4. The present study focuses on γ-$LiAlO_2$.

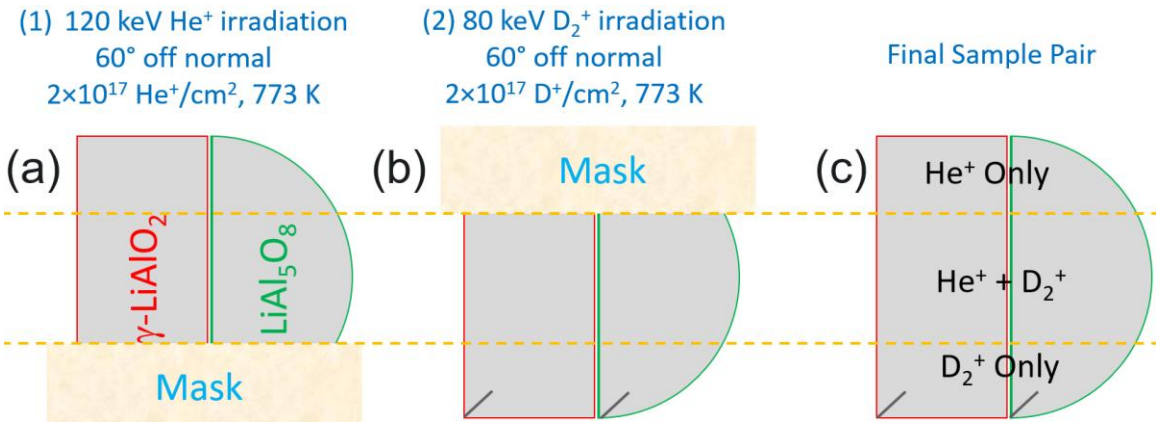


Figure 4. γ-$LiAlO_2$ and $LiAl_5O_8$ pellet samples irradiated using a mask: (a) 2×10^{17} He^+/cm^2 at 773 K and (b) irradiation with 2×10^{17} D^+/cm^2 at 773 K, producing (c) three distinct regions subjected to He^+-only, D^+-only, and sequential He^++D^+ irradiations.

Both irradiations were performed at an incidence angle of 60° relative to the surface normal to an ion fluence of 2×10^{17} He^+/cm^2 or D^+/cm^2 at a specimen temperature of 773 K. The irradiation temperature is higher than the 573 K used for neutron irradiation because the ion-irradiation dose rates are approximately three orders of magnitude higher. The elevated temperature was therefore selected to facilitate thermally activated defect processes and better emulate the microstructural evolution associated with neutron irradiation [7]. The combined dose rates for sequential He^+ and D_2^+ irradiation were 3.8×10^{-4} and 1.5×10^{-4} dpa/s, as summarized in Table 1. To achieve a high deuterium flux, a D_2^+ molecular beam was employed instead of a D^+ ion beam. Upon entering the solid, each 80 keV D_2^+ molecular ion dissociates into two 40 keV D^+ ions of equal kinetic energy, thereby producing the equivalent irradiation conditions while increasing the ion flux. The relatively low ion energies and 60° incidence angle were deliberately selected to facilitate subsequent depth profiling of implanted species and irradiation-induced

damage. Magnetic beam rastering was applied to achieve spatially uniform irradiation over the targeted area. The irradiation was manually paused approximately every 15 minutes to check the beam current, and the measurements obtained during each interval were arithmetically averaged to estimate the corresponding dose rate. Despite this procedure, the total ion fluence is subject to an uncertainty of ~10% or greater. Prior to irradiation, the pellets were heated to 773 K using a filament positioned behind the copper sample holder.

2.3. Sample characterization

The irradiated pellets for post-irradiation characterization are shown in Fig. 5. Following irradiation, the pellets were sealed in an Ar-filled glass vial and secured with tape to minimize material degradation prior to characterization.

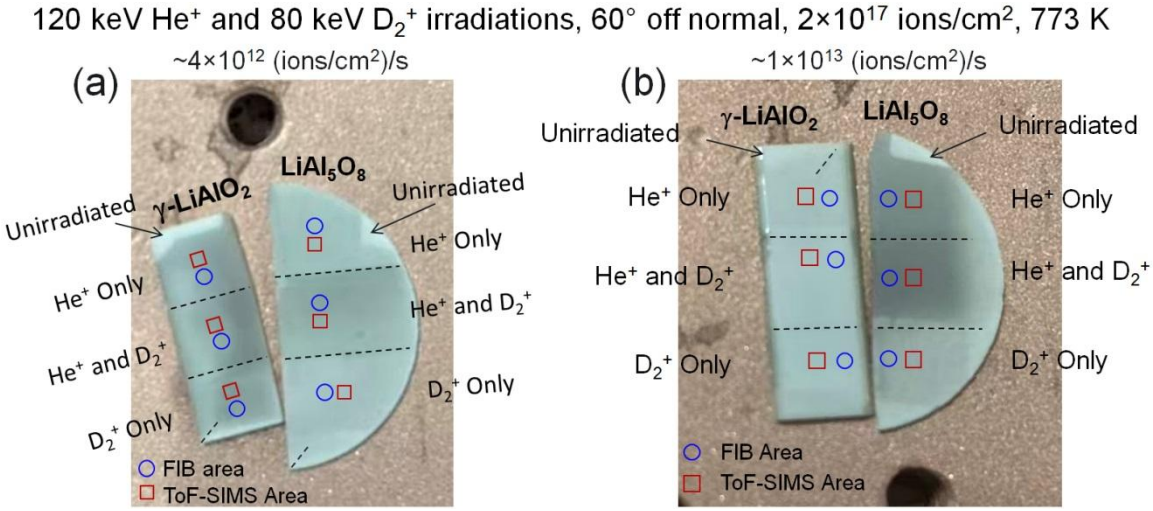


Figure 5. Ion-irradiated γ-$LiAlO_2$ and $LiAl_5O_8$ pellets at fluxes of (a) ~4×10^{12} and (b) ~1×10^{13} (ions/cm^2)/s, showing the locations selected for ToF-SIMS depth profiling (red squares) and FIB lift-out for STEM characterization (blue circles) within the three distinct irradiation regions.

Chemical depth profiling of the irradiated γ-$LiAlO_2$ pellet was performed using time-of-flight secondary ion mass spectrometry (ToF-SIMS) with a TOF.SIMS5 instrument (IONTOF GmbH, Münster, Germany). Negative secondary ions corresponding to H, D, Li, O, and Al were collected in dual-beam, non-interlaced mode. Material removal was achieved using a 2.0 keV Cs^+ sputter beam with a current of 142-128 nA, rastered over a 200 × 200 μm^2 area to generate a uniform sputter crater. For analysis, a focused 25 keV Bi^+ primary ion beam (~1.40 pA, 10 kHz repetition rate, ~5 μm spot size) was rastered over a 50 × 50 μm^2 central area (128 × 128 pixels) within the sputtered region. This configuration ensured that data were collected from the flat-bottom region of the crater while minimizing contributions from crater-edge effects. Each depth-profiling cycle consisted of 10.0 s of sputtering, followed by a 2.0 s pause and 3.28 s of data acquisition (two scans). To mitigate surface charging during analysis, a 10 eV electron flood gun was employed for charge compensation. In addition, a ~15 nm gold film was deposited on the pellet backside to improve conductivity and enhance signal intensity [11]. Multiple regions were analyzed

to assess measurement reproducibility and identify potential local inhomogeneities. The depth of the sputtered craters was measured using a Veeco Dektak 150 stylus profilometer, providing a depth calibration accuracy on the order of several nanometers.

Cross-sectional scanning transmission electron microscopy (STEM) specimens were prepared from the irradiated γ-$LiAlO_2$ pellets using an FEI Helios 600 NanoLab dual-beam focused ion beam (FIB) system. To protect the surface regions of interest from ion-beam damage during milling, an ~300 nm thick Pt layer electron-beam–deposited platinum was first deposited using the electron beam, followed by ~4 μm of carbon deposition on top of the Pt layer. Standard Ga^+ ion-beam lift-out procedures were then used to extract site-specific lamellae, which were subsequently mounted onto copper support grids. The lamellae were progressively thinned using decreasing Ga^+ accelerating voltages, with the final thinning performed at 5 kV to a thickness of ~100 nm. This procedure provided electron-transparent specimens while minimizing Ga^+-induced damage.

The specimens were examined in a ThermoFisher Scientific aberration-corrected Spectra Ultra STEM operated at 300 kV. High-angle annular dark-field (HAADF) STEM imaging was employed to characterize the irradiation-induced microstructures. To mitigate electron beam–induced damage and sample heating, low-dose imaging conditions were used, with a beam current of 20 pA and a dwell time of ~1 μs per pixel. Approximately 20 sequential, spatially overlapping images were acquired and frame-averaged to improve the signal-to-noise ratio while preserving the integrity of the irradiation-induced microstructure.

3. Results and Discussion

3.1. Deuterium retention and lithium depletion

Figure 6 presents the ToF-SIMS depth profiles of deuterium and lithium in a γ-$LiAlO_2$ pellet following He^+-only, D_2^+-only, and sequential He^+ and D_2^+ irradiations performed at 773 K in different regions of the same pellet to 2×10^{17} He^+/cm^2, 2×10^{17} D^+/cm^2, and 2×10^{17} $(He^+ + D^+)/cm^2$ at dose rates of 3.1×10^{-4}, 9.1×10^{-5}, and 3.8×10^{-4} dpa/s, respectively. To facilitate quantitative comparison among the different irradiation conditions, the measured D sputtering yields were normalized to the corresponding Al secondary-ion intensities, assuming that the Al concentration profile remains essentially unchanged in the material during irradiation. This normalization procedure reduces possible variations from fluctuations in the primary ion beam current and provides a more consistent measure of the relative non-gas D concentration and its depth distribution. The uncertainty in the measured D concentrations, dominated primarily by counting statistics, is estimated to be only a few percent. It is important to note that the D profiles measured by ToF-SIMS represent the atomic D retained in the solid rather than the total implanted D inventory. During sputtering, molecular D_2 gas trapped in irradiation-induced cavities or microcracks can be released readily upon rupture and therefore contributes only minimally to the detected D signal. The measured D concentration reflects primarily interstitial D and D bound to irradiation-induced defects, such as vacancies, vacancy clusters, and He-containing defect complexes. Thus, the integrated D signal provides an estimate of the non-gas D retention in the γ-$LiAlO_2$ matrix, whereas the total amount of implanted D may be higher if a significant fraction is present as molecular gas in cavities or other open-volume features.

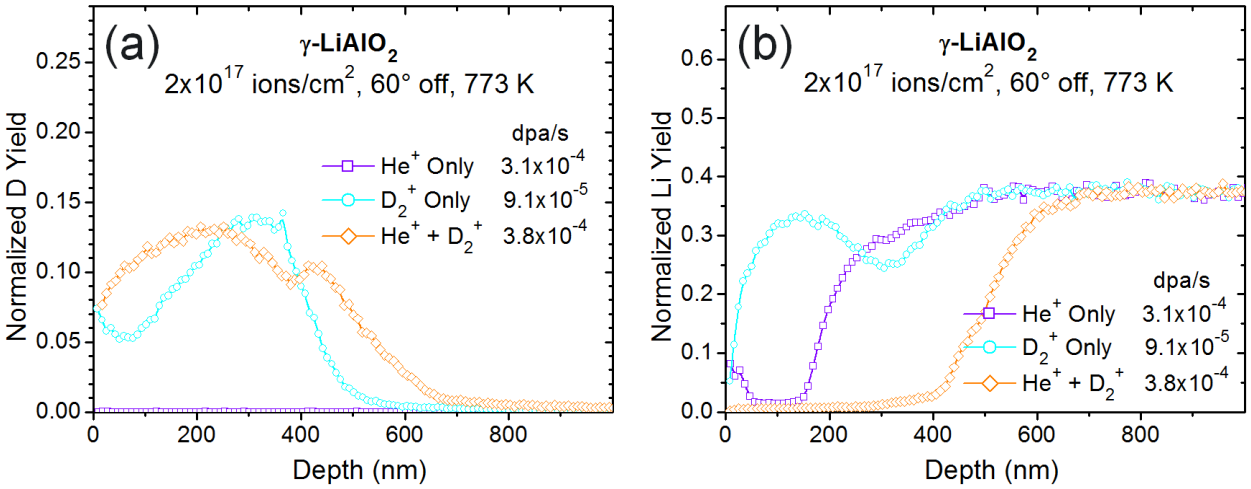


Figure 6. ToF-SIMS depth profiles of normalized (a) D/^{27}Al and (b) Li/^{27}Al yields in γ-$LiAlO_2$ pellets irradiated at 773 K to a fluence of 2×10^{17} ions/ cm^2 with He^+ only, D_2^+ only, and sequential He^++D_2^+ irradiation at dose rates of 3.1×10^{-4}, 9.1×10^{-5}, and 3.8×10^{-4}, respectively.

As shown in Fig. 6(a), the D profiles exhibit pronounced deviations from a simple Gaussian implantation distribution for both irradiation conditions. In particular, the broad and asymmetric profiles indicate that the implanted D does not remain confined to the region predicted solely by the ballistic implantation profile. Instead, D can migrate through the γ-$LiAlO_2$ lattice during irradiation at 773 K and subsequently become trapped at energetically favorable defect sites. The non-Gaussian profiles therefore reflect the combined effects of implantation, thermally activated D diffusion, defect-mediated trapping, and possible release from shallow trapping sites or migration toward microstructural sinks.

The integrated area under the D depth profile indicates that the non-gas D retention is substantially higher in the region that received prior He^+ irradiation than in the region irradiated with D_2^+ alone. This result demonstrates that He^+ irradiation promotes the formation of stable trapping sites for subsequently implanted D. At 773 K, He atoms and irradiation-induced vacancies can interact to form He–vacancy complexes and larger He-containing vacancy clusters. These complexes are expected to be more stable than isolated vacancies and can provide energetically favorable trapping sites for mobile D atoms during the subsequent D_2^+ irradiation. Consequently, a larger fraction of the implanted D remains associated with irradiation-induced defects when He irradiation precedes D implantation. In contrast, in the absence of implanted He, a fraction of the irradiation-produced vacancies can recombine with mobile interstitial atoms, migrate to grain boundaries, or be absorbed at internal and external surfaces. These recovery and sink processes reduce the population of stable vacancy-type defects available for D trapping. The lower D retention measured after D_2^+-only irradiation is therefore consistent with a lower density of stable trapping sites in the absence of pre-existing He-related defects. The enhanced D retention following sequential He^+ and D_2^+ irradiation provides direct evidence that He-induced defect structures can increase the capacity of γ-$LiAlO_2$ to retain atomic D at elevated temperature. The broader D distribution observed after prior He irradiation is consistent with enhanced D transport followed by trapping at the more stable He-associated defects.

Figure 6(b) shows the corresponding Li depth profiles. Li depletion is observed under all three irradiation conditions, demonstrating that Li is particularly susceptible to irradiation-induced redistribution and loss at a high dose rate and elevated temperature. The extent of Li depletion, however, depends strongly on the specific irradiation conditions. The most pronounced Li loss occurs following sequential He^+ and D_2^+ irradiation, where the Li intensity is nearly completely depleted within ~300 nm from the surface. A substantial but thinner depletion layer, ~170 nm in thickness, is also observed following He^+-only irradiation. These observations indicate that He irradiation strongly modifies the near-surface defect structure and enhances Li redistribution or transport under the subsequent irradiation conditions. The D_2^+-only condition produces the smallest overall Li loss caused by irradiation-induced interstitial production and diffusion. At 773 K, radiation-enhanced diffusion can be important because Li is highly mobile relative to the heavier cation sublattice. Compared to He^+-only irradiation, the substantially greater Li depletion observed after sequential He^+ and D_2^+ irradiation is a direct result of generation of additional Li interstitials by subsequent D_2^+ irradiation. In addition, irradiation-enhanced diffusion and thermally activated diffusion of Li interstitials could promote their transport in the irradiated material, producing a much broader Li-depleted region than that observed under either irradiation condition alone.

Taken together, the D and Li depth profiles demonstrate that He^+ irradiation has two important consequences for γ-$LiAlO_2$ at 773 K: it promotes the formation of stable defect structures that enhance subsequent non-gas D retention, while simultaneously modifying cation redistribution and Li loss near the irradiated surface. The correlation between enhanced D retention and increased Li depletion in the sequentially irradiated region highlights the coupled nature of defect evolution, D transport, and Li mobility under the irradiation conditions.

3.2. Microstructural features

3.2.1. He^+ irradiation

A micrometer-sized crystalline grain in a γ-$LiAlO_2$ pellet was examined using a FIB-prepared cross-sectional TEM specimen extracted from a region irradiated with He^+ ions to a fluence of 2×10^{17} He^+/cm^2 at 773 K and a relatively high dose rate of 3.1×10^{-4} dpa/s. The microstructure was characterized by both STEM and TEM, as shown in Figs. 7(a) and 7(b), respectively. Prior to imaging and diffraction analysis, the grain was manually oriented with respect to the incident electron beam to obtain a well-defined crystallographic orientation. Selected-area electron diffraction (SAED) patterns acquired from the irradiated and unirradiated regions are shown in Figs. 7(c) and 7(d), respectively. Comparison of the experimental diffraction patterns with simulated diffraction patterns indicates that the (004) and (020) reflections are expected for the observed orientation. Analysis of the measured *d*-spacings determines that the grain is oriented to the [100] zone axis. As shown in Fig. 7(a), several distinct irradiation-induced microstructural features can be identified, including He blisters, a polycrystalline region containing precipitates and cavities below the blister region, and a transition region exhibiting pronounced lattice-strain contrast adjacent to the underlying crystalline material. The thin, bright surface layer overlying the blisters is Ga contamination introduced during FIB specimen preparation and is not associated with irradiation-induced microstructural evolution or compositional changes.

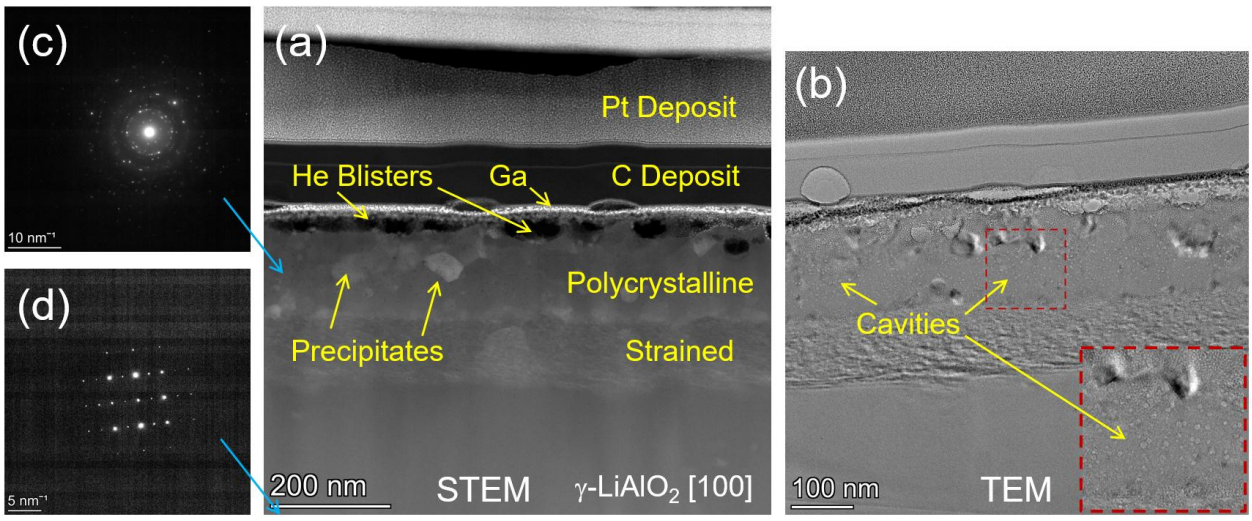


Figure 7. (a) STEM and (b) TEM micrographs showing the microstructure of a [100]-oriented γ-$LiAlO_2$ pellet irradiated to 2×10^{17} He^+/cm^2 at 773 K at a dose rate of 3.1×10^{-4} dpa/s. SAED patterns from the (c) irradiated and (d) featureless regions.

The formation of the He blisters is attributed to the implantation, diffusion, and trapping of He in irradiation-induced vacancy-type defects. At 773 K, the relatively high mobility of He and point defects promotes the formation and growth of He–vacancy complexes and larger vacancy clusters. As these complexes accumulate beneath the surface, they can grow and coalesce into gas-filled cavities and eventually produce blisters. The observed blisters range from several tens to several hundreds of nanometers in lateral dimensions, with some neighboring cavities interconnected to form elongated or irregularly shaped features. The morphology and distribution of these features are more clearly resolved in the higher-magnification image presented in Fig. 8. Immediately beneath the blister region, a polycrystalline layer ~170 nm thick is observed, which is highly Li depleted, as suggested by Fig. 6(b). This layer contains a high density of nanoscale precipitates with a broad range of morphologies and sizes, from a few nanometers to several tens of nanometers. The precipitates exhibit brighter contrast than the surrounding matrix in the STEM images, suggesting a higher average atomic number (Z) in the precipitate composition. Based on our previous studies [2, 12, 13] of ion irradiated γ-$LiAlO_2$ pellets, the enhanced contrast is likely a result of the formation of a non-stoichiometric $LiAl_5O_8$-type phase. However, the compositional and phase identification of these nanoscale precipitates requires complementary analytical measurements and should therefore be considered tentative based solely on the observed Z-contrast. In addition to the precipitates, a high density of small irradiation-induced cavities is distributed throughout the polycrystalline layer, as shown more clearly in Fig. 8. This selected polycrystalline region contains grain boundaries. However, the cavities appear to be distributed relatively uniformly throughout the irradiated polycrystalline layer. There is no obvious preferential accumulation of larger cavities at the grain boundaries. This observation suggests that, under the present irradiation conditions, grain boundaries do not act as dominant cavity sinks.

There is a transition region with distinct lattice-strain contrast between the polycrystalline layer and the underlying material. This region is formed as a result of competition between defect production through both electronic and elastic collision processes and simultaneous defect recovery driven by

irradiation-enhanced and thermally activated diffusion during ion irradiation at 773 K. No obvious precipitates or irradiation-induced cavities are observed in this transition region. At greater depths, the microstructure appears essentially featureless; however, non-gas D was detected [Fig. 6(a)], indicating trapping at possible He-vacancy clusters. The presence of similar defect clusters in a γ-$LiAlO_2$ pellet irradiated to 2×10^{17} $(He^+ + D^+)/cm^2$ at 773 K was confirmed by positron annihilation spectroscopy (PAS) [14]. The preservation of the crystalline microstructure and the absence of detectable cavities at greater depths suggest that defect production and recovery are nearly balanced in this region. Overall, the cross-sectional TEM observations demonstrate that He^+ irradiation of γ-$LiAlO_2$ at 773 K produces a highly heterogeneous microstructure consisting of He blisters, an ~170-nm-thick polycrystalline, Li-depleted layer containing Al-rich precipitates and abundant nanoscale cavities, an ~90 nm-thick lattice-strained transition region, and a deeper, featureless crystalline matrix in which non-gas D remains trapped.

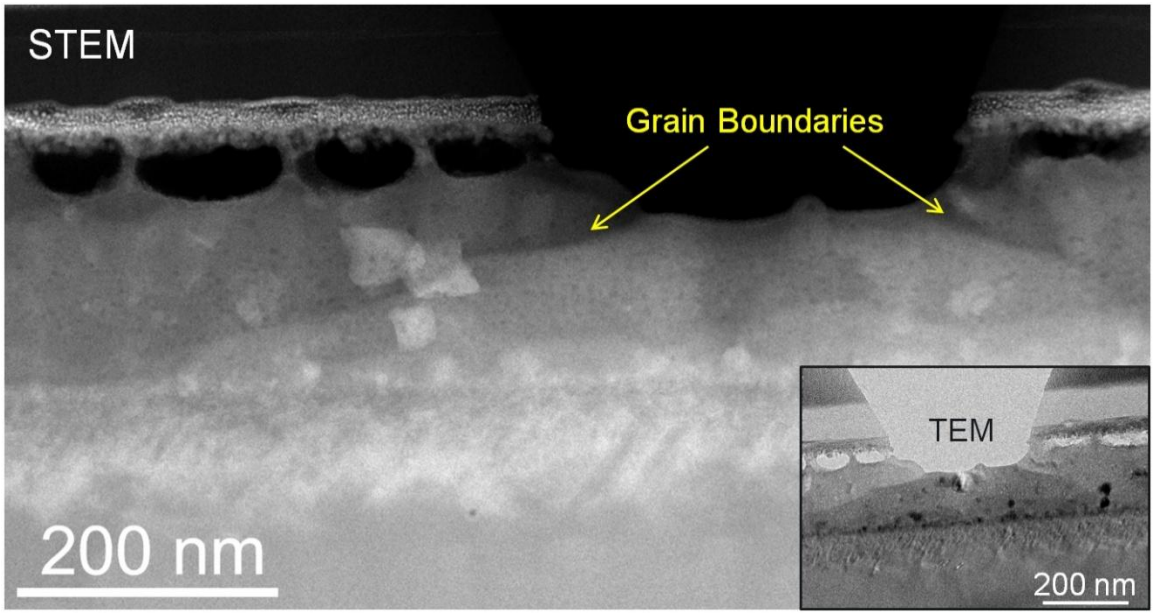


Figure 8. A STEM micrograph, with an inset TEM image, showing a grain-boundary region in a γ-$LiAlO_2$ pellet irradiated to 2×10^{17} He^+/cm^2 at 773 K at a dose rate of 3.1×10^{-4} dpa/s.

3.2.2. D_2^+ irradiation

Figure 9 presents the microstructure of a [001]-oriented γ-$LiAlO_2$ grain irradiated with D_2^+ ions to a fluence of 2×10^{17} D^+/cm^2 at 773 K and a dose rate of 9.1×10^{-5} dpa/s. In contrast to the He^+-irradiated microstructure described above, the D_2^+-irradiated region retains an ~160 nm thick monocrystalline surface region, beneath which a distinct layer containing large, faceted precipitates and associated cavities is formed, as shown in Fig. 9(a). The preservation of crystallinity in the near-surface region indicates that dynamic recovery at 773 K remains sufficiently effective to prevent polycrystallization under the present D_2^+ irradiation conditions. At greater depth, however, the irradiation-induced redistribution of Li and the accumulation of vacancy-type defects result in pronounced precipitation and cavity formation.

The precipitates exhibit a broad size distribution, ranging from a few nanometers to several hundred nanometers, and many have well-defined faceted morphologies. Based on their morphology, Li depletion [Fig. 6(b)], and the phase behavior previously observed in γ-$LiAlO_2$ under ion irradiation [2, 12, 13], these precipitates are tentatively identified as a non-stoichiometric $LiAl_5O_8$-type phase. The precipitate-containing region is centered at a depth of ~240 nm and has a thickness of ~160 nm. Considering the irradiation-induced volumetric swelling in the top surface layer, the spatial localization of this precipitate-cavity layer is consistent with the peak region of D_2^+ irradiation-induced displacement damage, and suggests that the precipitation process is closely associated with the mobile Li interstitials produced by D_2^+ irradiation. The formation of the $LiAl_5O_8$ precipitates can be understood in terms of irradiation-induced Li redistribution. D_2^+ irradiation produces displacement damage and associated point defects, while the elevated temperature of 773 K provides sufficient mobility for Li to diffuse over relatively long distances. Li migration away from the damaged region can locally drive the γ-$LiAlO_2$ matrix toward a Li-deficient composition. Under such conditions, formation of the cubic $LiAl_5O_8$ phase becomes thermodynamically favorable because it accommodates a lower Li concentration than stoichiometric γ-$LiAlO_2$. The precipitation process can therefore be viewed as a coupled sequence of radiation-induced defect production, Li diffusion, local compositional deviation from the parent phase, and subsequent precipitation of a Li-deficient Al-rich phase. The broad precipitate size distribution further suggests that nucleation and growth occur concurrently during irradiation, with larger precipitates developing through continued solute redistribution and coarsening at 773 K.

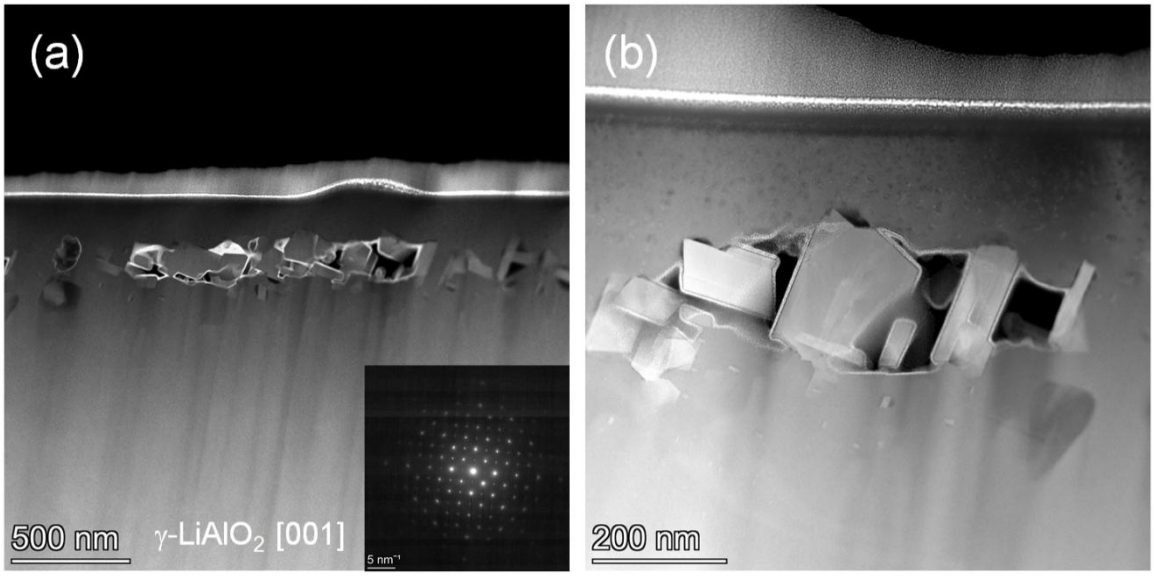


Figure 9. STEM micrographs showing the microstructure of a [001]-oriented γ-$LiAlO_2$ pellet irradiated to 2×10^{17} D^+/cm^2 at 773 K at a dose rate of 9.1×10^{-5} dpa/s, at (a) low and (b) higher magnifications. The inset in (a) shows a SAED pattern from an unirradiated region.

The large cavities surrounding the precipitates are another prominent feature of the D_2^+-irradiated microstructure. Their formation is likely associated with the accumulation and clustering of vacancies generated during irradiation. In particular, the redistribution of Li can produce excess Li interstitials and

corresponding vacancy populations in the surrounding matrix. At 773 K, these vacancies are sufficiently mobile to migrate, interact, and form stable vacancy clusters that subsequently evolve into larger cavities. The spatial association between the large precipitates and cavities suggests that precipitation and vacancy evolution are strongly coupled. Local chemical redistribution may alter defect formation and migration energetics, while the precipitation process itself can provide additional sinks or interfaces for point defects. Thus, the observed precipitate–cavity structure likely results from the simultaneous evolution of chemical composition and irradiation-induced open volume rather than from independent precipitation and cavity-nucleation processes.

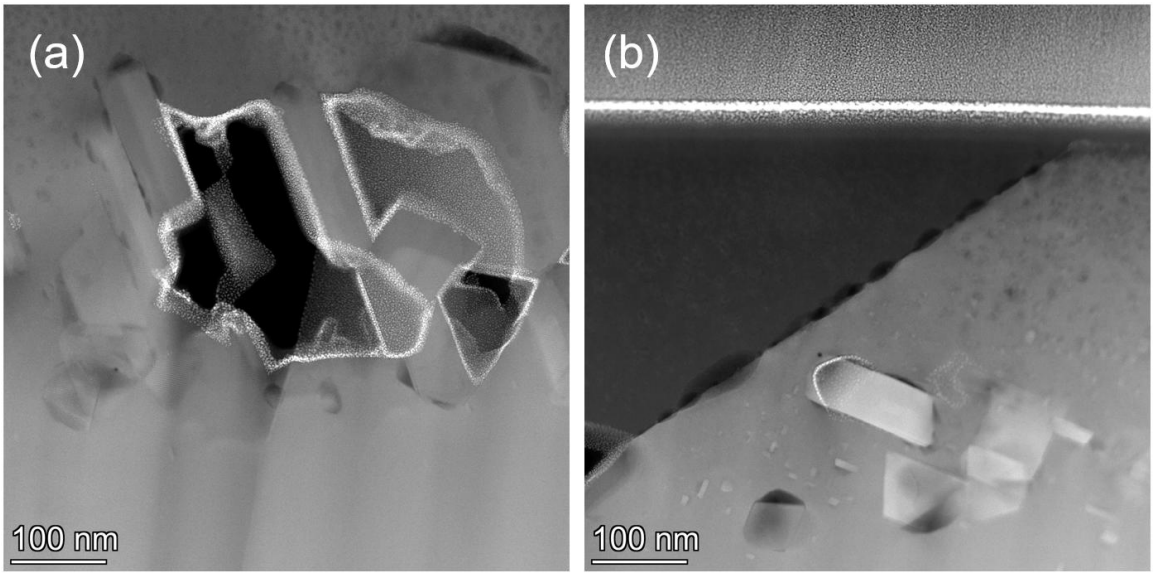


Figure 10. (a) STEM micrographs showing (a) precipitates breaking and relocating to create a large void and (b) a grain-boundary with preferential formation of cavities in a γ-$LiAlO_2$ pellet irradiated to 2×10^{17} D^+/cm^2 at 773 K at a dose rate of 9.1×10^{-5} dpa/s.

Higher-resolution STEM images in Fig. 10(a) provide additional details of this complex microstructure. Several precipitates appear to have fractured, detached, and been displaced during or after FIB specimen preparation, leaving relatively large empty regions in the cross-sectional specimen. These apparent voids should therefore not necessarily be interpreted as irradiation-induced cavities. Instead, their morphology and location are consistent with the mechanical removal or pull-out of weakly bonded or loosely supported precipitates during thinning and subsequent handling of the FIB lamella. This distinction is important when estimating the actual cavity volume fraction from the STEM images. The intact regions surrounding these preparation-induced gaps nevertheless clearly demonstrate the close association between the large precipitates and the irradiation-induced cavity population.

In addition to the large cavities surrounding the precipitates, a high density of much smaller cavities, typically only a few nanometers in size, is observed within the monocrystalline surface layer. The presence of these nanoscale cavities indicates that vacancy clustering occurs even in the region where the γ-$LiAlO_2$ crystal structure remains largely intact. This behavior is qualitatively similar to the high density of small cavities observed in the polycrystalline layer produced by He^+ irradiation [Fig. 8]. The difference

is that, under D_2^+ irradiation, no large blisters are formed and cavities in the deep damaged region evolve into much larger features in the precipitate-containing layer. This depth-dependent cavity evolution may reflect differences in defect production, gas species transport, local Li concentration, and the balance between defect recombination and defect clustering. Interestingly, no obvious cavities are observed within the nanoscale $LiAl_5O_8$ precipitates themselves. Instead, the cavities are concentrated in the surrounding matrix. This observation suggests that vacancies generated during irradiation may readily migrate to the precipitate/matrix interfaces. The absence of cavities inside the precipitates, together with their strong association with the precipitate interfaces, further supports a coupled relationship between precipitation and vacancy redistribution.

Figure 10(b) shows the D_2^+-irradiated microstructure in a region containing a grain boundary. Large cavities are preferentially formed along the grain boundary. The strong grain-boundary segregation of cavities indicates that grain boundaries act as efficient sinks for irradiation-induced vacancies and provide favorable sites for vacancy accumulation and cavity nucleation. The preferential cavity formation at the grain boundary under D_2^+ irradiation contrasts markedly with the He^+-irradiated microstructure shown in Fig. 8, where no clear evidence of preferential grain-boundary cavity accumulation was observed. Instead, large He blisters formed beneath the surface. This difference could originate from specific boundary properties that exhibit different sink strength for vacancies and gas species.

Another notable feature of the microstructure is the absence of an obvious strained transition region between the precipitate-containing layer and the underlying unirradiated crystalline material. In contrast to the He^+-irradiated specimen, where a distinct region of lattice-strain contrast was observed adjacent to the polycrystalline layer, the D_2^+-irradiated specimen exhibits a comparatively sharp transition from the precipitate-containing region to the underlying crystalline γ-$LiAlO_2$. This difference may reflect the distinct defect evolution pathways associated with He^+ and D_2^+ irradiations. In particular, He atoms can stabilize vacancy clusters and promote the development of a highly damaged polycrystalline layer, whereas D_2^+ irradiation at the present dose rate appears to favor recovery and retention of crystallinity accompanied by localized Li redistribution and precipitation.

Overall, the D_2^+-irradiated γ-$LiAlO_2$ microstructure is characterized by a distinct combination of retained crystallinity, irradiation-induced Li redistribution, $LiAl_5O_8$-type precipitation, and cavity formation. The formation of large faceted Li-deficient precipitates surrounded by large cavities in the peak-damage region, together with preferential cavity accumulation at grain boundaries, demonstrates that D_2^+ irradiation at 773 K promotes a defect evolution pathway substantially different from that produced by He^+ irradiation. These results further emphasize the important role of irradiation species, defect chemistry, and microstructural sinks in controlling phase stability and cavity evolution in γ-$LiAlO_2$.

3.2.3. Sequential He^+ and D_2^+ irradiation

Under sequential He^+ and D_2^+ irradiation to a total fluence of 2×10^{17} $(He^+ + D^+)/cm^2$ at 773 K and a dose rate of 3.8×10^{-4} dpa/s, the γ-$LiAlO_2$ pellet develops a highly heterogeneous near-surface microstructure. The primary features include a completely amorphized surface layer ~280 nm thick, followed by a distinct layer containing non-stoichiometric $LiAl_5O_8$-type precipitates and irradiation-induced cavities. A representative cross-sectional overview is shown in Fig. 11, together with SAED patterns obtained from the irradiated and unirradiated regions. The diffraction patterns confirm the amorphous nature of the surface layer and the [101] crystallographic orientation of the analyzed grain,

respectively. The near-surface region, which experiences the highest electronic excitation and ionization induced by energetic ions, evolves into complete amorphization and contains abundant nanoscale cavities. At greater depth, where subsequent D transport and radiation-enhanced diffusion remain significant, Li redistribution and precipitation dominate, resulting in the formation of $LiAl_5O_8$-type precipitates accompanied by cavity formation. The resulting structure is therefore a consequence of the spatially coupled evolution of displacement damage, gas transport, defect clustering, chemical redistribution, and phase transformation.

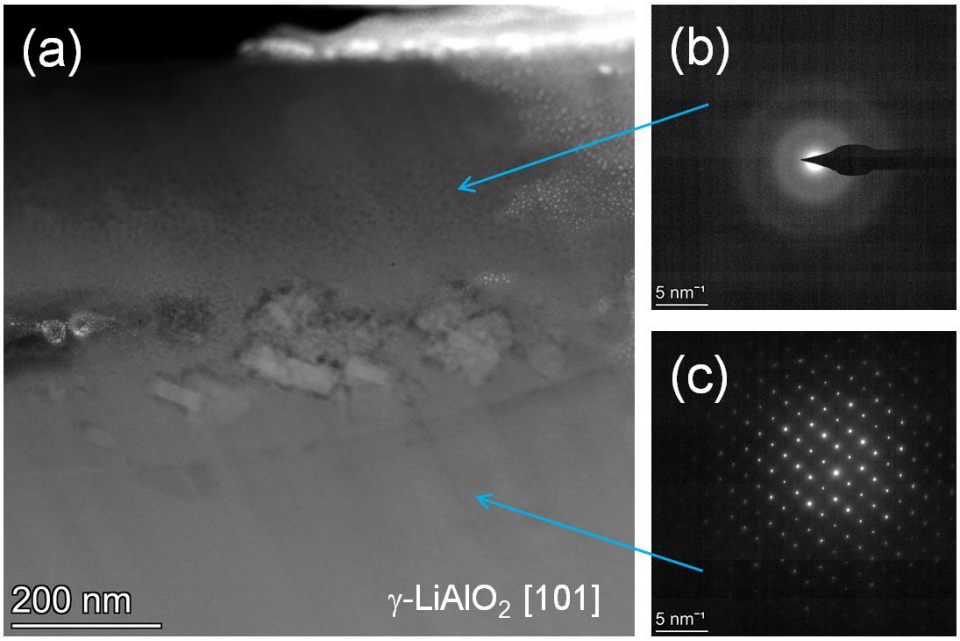


Figure 11. (a) STEM micrograph showing the microstructure of a [101]-oriented γ-$LiAlO_2$ pellet irradiated to 2×10^{17} $(He^+ + D^+)/cm^2$ at 773 K at a dose rate of 3.8×10^{-4} dpa/s. (b) and (c) SAED patterns from the irradiated and unirradiated regions, respectively.

The overall microstructure is consistent with our previous observations, including the representative structure shown in Fig. 2(b). Several distinct microstructural features have been identified [2] from the surface toward the unirradiated matrix. Depending on grain orientation, grain-boundary character, and local defect-sink conditions, medium- to high-dose-rate sequential irradiation produces a combination of complete surface amorphization, an apparent gas-filled fracture or delamination feature, a deeper precipitate-cavity-containing region, cavity aggregation at grain boundaries, and denuded zones adjacent to grain boundaries. The precipitates consist primarily of non-stoichiometric $LiAl_5O_8$-type precipitates surrounded by cavities [2]. The substantial variation in the morphology and spatial extent of these features from grain to grain indicates that irradiation damage is strongly influenced by local microstructural conditions. In particular, grain boundaries can provide efficient pathways for defect and gas transport, whereas crystallographic orientation may affect both defect accumulation and the kinetics of radiation-induced precipitation.

The deeper precipitate-cavity-containing layer can likewise be understood in terms of the pre-existing microstructure created during the He^+ irradiation. The He^+ irradiation produces a transition region beneath the polycrystalline layer and an underlying featureless microstructure containing non-gas D trapped at defect clusters. Subsequent D_2^+ irradiation provides additional displacement damage and introduces a highly mobile species at 773 K. D_2^+-induced enhancement of Li mobility can drive Li redistribution away from the damaged region, producing locally Li-deficient compositions that favor the formation of non-stoichiometric $LiAl_5O_8$-type precipitates. At the same time, vacancy accumulation associated with radiation damage and Li redistribution promotes cavity nucleation and growth around the precipitates. The observed precipitate-cavity layer therefore likely represents the evolved form of the He-induced damage region following additional D_2^+ irradiation.

The transport and accumulation of He and D are also expected to play an important role in producing the complex gas-related features observed in the sequentially irradiated specimen. Gas mobility is strongly affected by the local defect structure, vacancy concentration, grain boundaries, and interfaces. Depending on the local microstructural environment, implanted gas atoms may remain trapped within defect clusters, diffuse toward the surface, accumulate at grain boundaries, or contribute to the growth of larger cavities. These competing transport pathways can produce distinctly different morphologies, including He blisters, gas-filled fractures or delamination features, and preferential cavity aggregation along grain boundaries. The apparent gas-filled fracture separating the amorphized surface region from the deeper precipitate-cavity layer [Fig. 2(b)] may represent a local high-gas-concentration region.

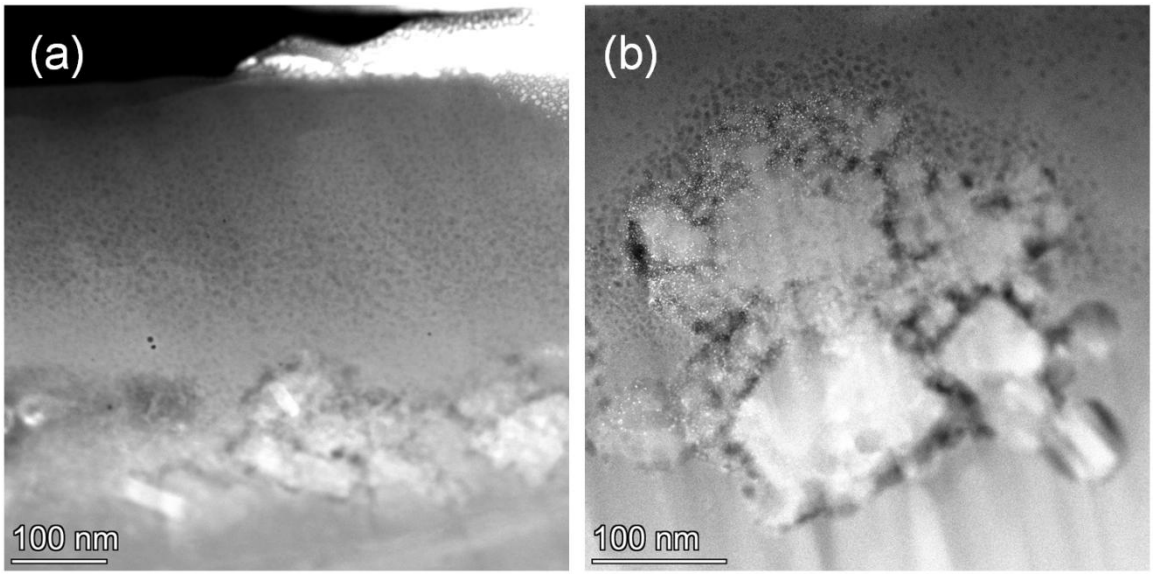


Figure 12. STEM micrographs showing precipitates and cavities in a γ-$LiAlO_2$ pellet irradiated to 2×10^{17} $(He^+ + D^+)/cm^2$ at 773 K at a dose rate of 3.8×10^{-4} dpa/s, at (a) low and (b) higher magnifications.

The amorphized layer contains a high density of nanoscale cavities, which are more clearly resolved in the higher-magnification STEM image shown in Fig. 12(a). The coexistence of amorphization and abundant cavities indicates that cavity nucleation and growth can proceed even after long-range crystalline order has been lost. The ToF-SIMS results in Fig. 6(b) further show that this near-surface

region is strongly Li depleted. The severe Li depletion is consistent with the high defect concentration and enhanced Li mobility expected in the amorphized layer at 773 K. Radiation-enhanced Li transport toward the surface may contribute to the substantial compositional change, while the loss of Li can further destabilize the γ-$LiAlO_2$ structure and promote amorphization and phase transformation.

Figure 12(b) provides a higher-resolution view of a region containing a population of apparently evolving precipitates and cavities. The microstructure exhibits a continuum of precipitate morphologies. Some precipitates have well-defined, faceted boundaries and are surrounded by relatively large cavities, whereas others exhibit poorly defined or diffuse interfaces and are associated with numerous smaller, spatially separated cavities. In several locations, the small cavities appear to be aligned or sufficiently close to one another that they could progressively coalesce into larger cavities. This morphological progression is consistent with a precipitation-and-cavity-growth process in which local compositional redistribution and vacancy clustering occur concurrently. The microstructural features in Fig. 12(b) provide particularly strong qualitative support for the proposed mechanism of coupled $LiAl_5O_8$ precipitation and cavity formation. An early stage may involve irradiation-induced Li redistribution and the formation of small Li-deficient regions, accompanied by the nucleation of small vacancy clusters. Continued irradiation and thermal diffusion allow these regions to evolve: the Li-deficient domains grow and develop into more clearly defined $LiAl_5O_8$-type precipitates, while nearby vacancy clusters migrate, coalesce, and grow into larger cavities. As precipitation proceeds, the interfaces between the secondary phase and γ-$LiAlO_2$ matrix may further influence vacancy and gas transport, promoting the preferential accumulation of cavities around the precipitates. The coexistence of poorly defined precipitates with isolated small cavities and well-faceted precipitates surrounded by larger cavities can therefore be interpreted as different stages of the same coupled microstructural evolution pathway.

Overall, the sequential He^+ and D_2^+ irradiation results demonstrate that the final microstructure is determined not simply by a superposition of the structures from individual He^+-only and D_2^+-only irradiation responses, but by the further irradiation of defect structure inherited from the preceding irradiation. He^+ irradiation establishes a defect-rich, partially transformed microstructure, while subsequent D_2^+ irradiation drives further damage accumulation, D transport, Li redistribution, precipitation, and cavity evolution. The resulting combination of amorphization, gas-filled fracture, $LiAl_5O_8$-type precipitation, and cavity formation highlights the strongly coupled nature of gas–defect interactions and chemical redistribution in γ-$LiAlO_2$ under elevated-temperature sequential irradiation.

3.2.4. Microstructural comparison

Figure 13 compares the microstructures of γ-$LiAlO_2$ pellets irradiated at 773 K under He^+-only, D_2^+-only, and sequential He^+ and D_2^+ conditions. The irradiation fluence was 2×10^{17} ions/cm^2 for each condition, with an ion flux of ~1×10^{13} (ions/cm^2)/s. The corresponding dose rates were 3.1×10^{-4} dpa/s for He^+ irradiation, 9.1×10^{-5} dpa/s for D_2^+ irradiation, and 3.8×10^{-4} dpa/s for sequential He^+ and D_2^+ irradiation. The STEM images were acquired from different crystallographic orientations, and the zone axes therefore differ among the three conditions. As demonstrated previously [7], a rigorous comparison of irradiation-induced microstructures is best performed using specimens oriented along the same crystallographic zone axis because diffraction contrast, defect visibility, and apparent feature morphology can depend on grain orientation. Unfortunately, suitable FIB-prepared specimens with comparable orientations were not obtained for all three irradiation conditions in the present study. Therefore, the comparison in Fig. 13 should be considered qualitative rather than a strict one-to-one comparison.

Nevertheless, the substantial differences among the three microstructures provide useful insight into the effects of irradiation sequence.

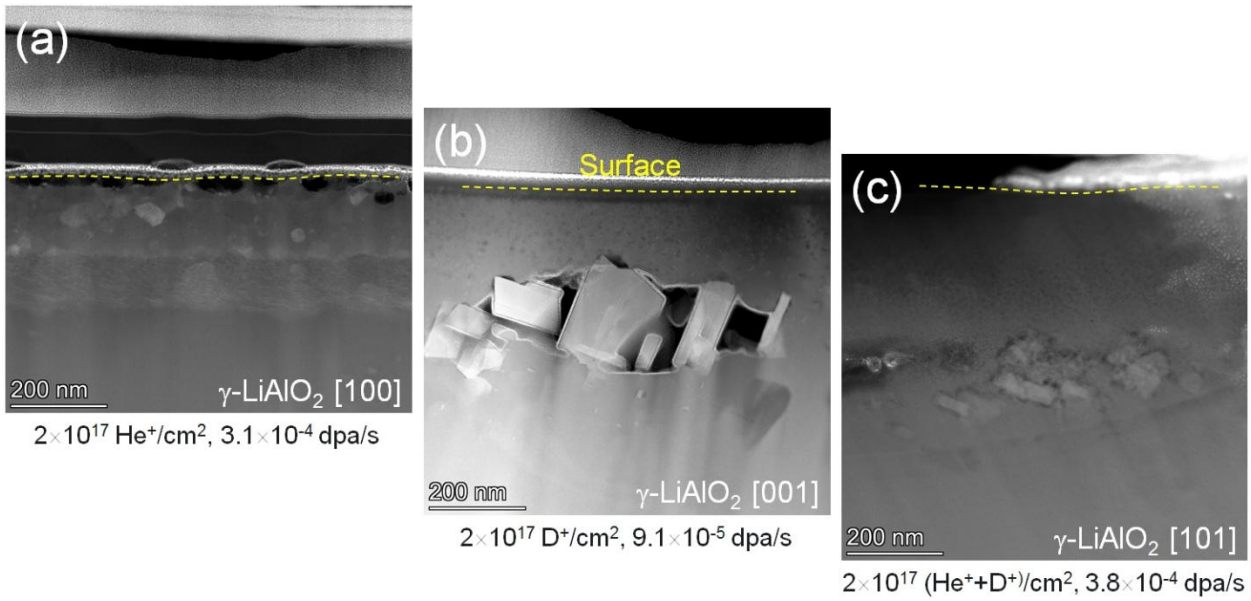


Figure 13. Comparison of STEM micrographs showing microstructures in γ-$LiAlO_2$ pellets irradiated at 773 K to (a) 2×10^{17} He^+/cm^2, (b) 2×10^{17} D^+/cm^2, and 2×10^{17} $(He^+ + D^+)/cm^2$ at an ion flux of ~1×10^{13} $(ions/cm^2)/s$.

As shown in Fig. 13(a) for the He^+-only condition, irradiation at 773 K produces He blisters, a polycrystalline layer containing precipitates and small cavities, and a deeper featureless region containing trapped non-gas D. In contrast, D_2^+-only irradiation [Fig. 13(b)] produces a relatively intact monocrystalline surface layer with cavities followed by a distinct precipitate-cavity-containing region. The precipitates in the D_2^+-only condition are generally large, ranging from several nanometers to hundreds of nanometers, and are associated with large cavities. These observations indicate that D_2^+ irradiation alone promotes substantial Li redistribution and precipitation at 773 K while allowing the surface region to retain its crystalline structure. The sequentially irradiated microstructure [Fig. 13(c)] is markedly different. Most of the microstructural features established during the preceding He^+ irradiation appear to have been further transformed by the subsequent D_2^+ irradiation. In particular, the near-surface region is completely amorphized to a depth of ~280 nm. This depth encompasses not only the polycrystalline region produced by He^+ irradiation but also the lattice strained crystalline region. The observation suggests that subsequent D_2^+ irradiation can drive the pre-existing He-damaged material beyond the damage-recovery threshold, resulting in complete loss of long-range crystalline order.

The most important observation is that the microstructure produced by sequential He^+ and D_2^+ irradiation cannot be interpreted simply as a superposition of the structures generated independently by He^+-only and D_2^+-only irradiation responses. Instead, the second irradiation step acts on a microstructure that has already been substantially modified by the first irradiation step. This distinction is particularly important for understanding the origin of the amorphous and precipitate-cavity-containing layers. The

formation of the extended amorphous layer is associated with continued D_2^+ irradiation of the defective and polycrystalline layer that was generated during the preceding He^+ irradiation. Subsequent D_2^+ irradiation introduces additional displacement damage and rupture of chemical bonds through electronic energy deposition into this already defective region. The additional damage, together with D transport and interactions with the pre-existing defect population, can disrupt the short- and medium-range crystalline order and ultimately drive the near-surface region into a fully amorphous state.

The fate of the He blisters after the subsequent D_2^+ irradiation cannot be established conclusively from the present observations. The apparent absence of the large He blisters observed after He^+-only irradiation may indicate that they were modified, destabilized, or released during D_2^+ irradiation. However, it is also possible that the particular FIB lift-out region examined did not intersect sufficiently large blisters. Therefore, additional site-specific characterization is required before concluding that the He blisters were completely eliminated.

Another important difference is observed in the precipitate-containing region. In the sequentially irradiated specimen, relatively small precipitates are distributed in the deeper region that largely overlaps the featureless region containing non-gas D trapped at defect clusters produced by the preceding He^+ irradiation. These precipitates are substantially smaller than the large, faceted precipitates formed during D_2^+-only irradiation in pristine crystal. This difference suggests that pre-existing He-induced defects modify the nucleation and growth of the secondary phase during subsequent D irradiation. The He^+-induced defect population may provide numerous nucleation sites while simultaneously altering Li transport pathways, vacancy concentrations, and local chemical potentials, thereby favoring the formation of a high density of smaller precipitates rather than the growth of fewer, much larger precipitates. The resulting defect accumulation, dynamic recovery, D trapping, gas transport, and Li redistribution produce a microstructure fundamentally different from that generated by either irradiation species alone.

3.3. Low dose-rate case

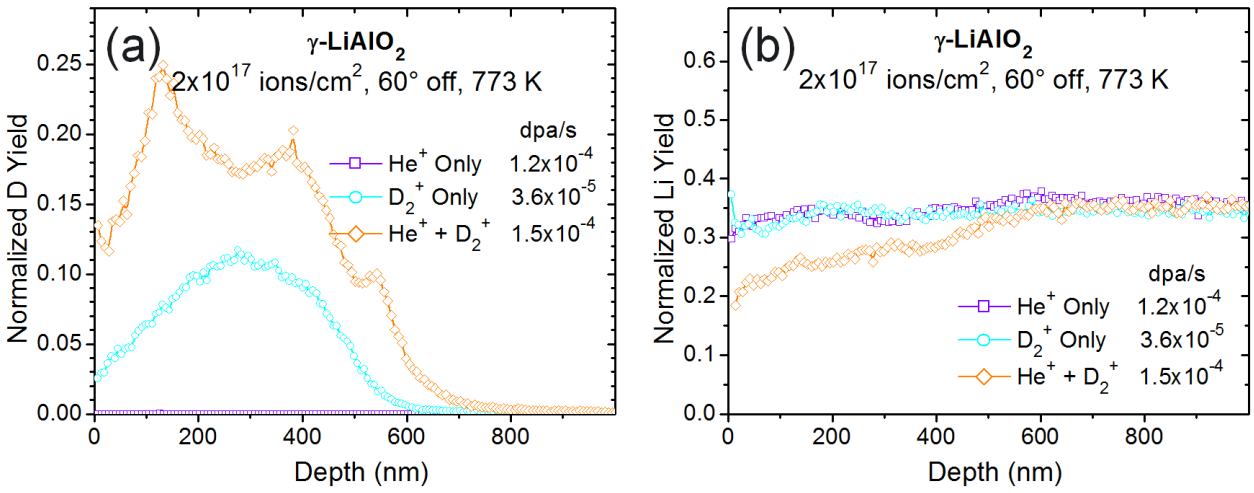


Figure 14. ToF-SIMS depth profiles of normalized (a) D/^{27}Al and (b) Li/^{27}Al in γ-$LiAlO_2$ pellets irradiated at 773 K to a fluence of 2×10^{17} ions/ cm^2 with He^+ only, D^+ only, and sequential He^++D^+ irradiation at a dose rate of 1.2×10^{-4}, 3.6×10^{-5}, and 1.5×10^{-4}, respectively.

For comparison of the irradiation-induced microstructures and deuterium behavior at different dose rates, a second set of irradiations was performed at a lower dose rate. Figure 14 presents the depth profiles of normalized D and Li in a γ-$LiAlO_2$ pellet irradiated at 773 K to 2×10^{17} He^+/cm^2, 2×10^{17} D^+/cm^2, and 2×10^{17} $(He^+ + D^+)/cm^2$ at dose rates of 1.2×10^{-4}, 3.6×10^{-5}, and 1.5×10^{-4} dpa/s, respectively. These experiments provide a direct comparison with the higher-dose-rate results presented in Fig. 6 and allow the effects of dose rate on D retention, Li redistribution, and irradiation-induced microstructural evolution to be evaluated under otherwise same temperature and fluence conditions.

As shown in Fig. 14(a), the non-gas D retention is substantially higher in the region that received prior He^+ irradiation than in the region subjected to D_2^+ irradiation alone. This behavior further demonstrates the important role of He^+ irradiation-induced defects in trapping D. Prior He^+ irradiation produces vacancies and He-vacancy complexes that can persist at 773 K and serve as stable trapping sites for mobile D introduced during the subsequent D_2^+ irradiation. In contrast, when D_2^+ irradiation is performed without prior He^+ implantation, a larger fraction of irradiation-induced vacancies can recombine with interstitials or migrate to microstructural sinks, reducing the population of stable defect sites available for D trapping.

Interestingly, the integrated non-gas D retention at the lower dose rate appears to be higher than that measured under the corresponding higher-dose-rate irradiation conditions. This dose-rate dependence suggests that the balance between defect production, defect recombination, D diffusion, and D trapping is strongly influenced by the rate at which displacement damage is introduced. At the lower dose rate, the longer time available between successive displacement-cascade events allows D atoms to migrate over greater distances and sample a larger population of energetically favorable trapping sites. At the same time, the slower accumulation of damage may promote the evolution of relatively stable He-vacancy complexes and other trapping centers rather than their rapid conversion into larger cavities that can confine D_2 gas. The enhanced non-gas D retention at the lower dose rate therefore likely reflects a more favorable competition between D transport and defect trapping. Nevertheless, because ToF-SIMS primarily measures non-gas D retained in the solid, the observed increase does not necessarily imply an increase in the total implanted D inventory; changes in the fraction of D present as molecular gas in cavities may also contribute to the difference.

The Li depth profiles shown in Fig. 14(b) exhibit a striking contrast with those obtained at the higher dose rate. No pronounced Li depletion is apparent following either He^+-only or D_2^+-only irradiation. A small reduction in the near-surface Li signal appears to be present following sequential He^+ and D_2^+ irradiation at the low dose rate, but the extent of Li loss is substantially smaller than that observed under the higher-dose-rate conditions [Fig. 6(b)]. These results indicate that significant Li redistribution is not an inevitable consequence of irradiation at 773 K and 2×10^{17} ions/cm^2; rather, the magnitude of Li transport depends strongly on the irradiation dose rate. The suppression of Li depletion at the lower dose rate may be related to enhanced defect recovery between irradiation events. At a lower production rate, point defects have more time to recombine, migrate to sinks, and approach a lower steady-state concentration. The defect population appears insufficient to produce the extensive Li depletion observed at the higher dose rate. The strong dose-rate dependence of Li redistribution is therefore consistent with a competition between defect production and dynamic recovery at 773 K.

The microstructure resulting from sequential He^+ and D_2^+ irradiation at the lower dose rate is shown in Fig. 15 and is similar to that presented previously in Fig. 2(a). In contrast to complete amorphization observed at the higher dose rate, the low-dose-rate specimen retains a crystalline surface layer. No continuous amorphous layer or large He blisters are observed. Instead, the near-surface region remains monocrystalline, followed by a distinct layer containing irradiation-induced precipitates and associated cavities at greater depth. The preservation of crystallinity is consistent with the absence of significant Li depletion in the ToF-SIMS measurements and suggests that dynamic defect recovery at the lower dose rate is sufficiently effective to suppress the extensive structural disorder and chemical redistribution observed at the higher dose rate.

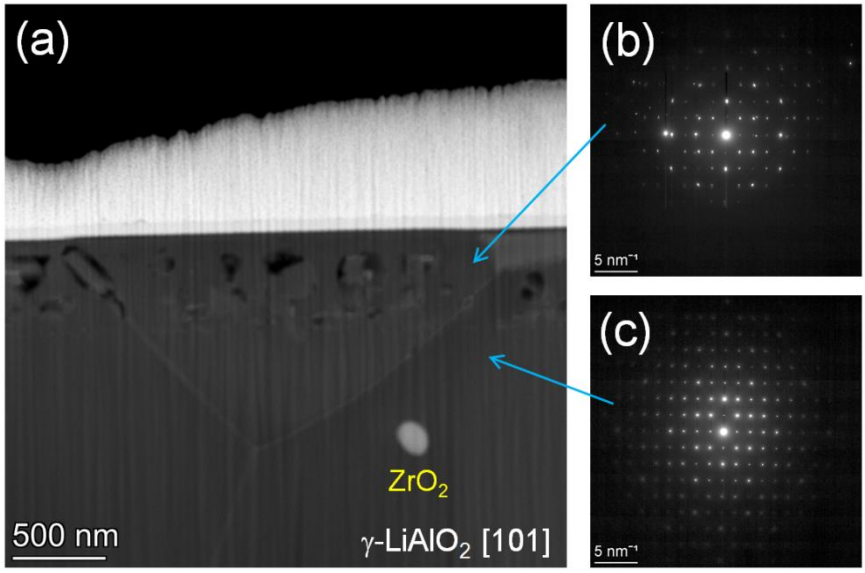


Figure 15. (a) A STEM micrograph showing the microstructure of a [101]-oriented γ-$LiAlO_2$ grain in a pellet irradiated at 773 K to 2×10^{17} $(He^+ + D^+)/cm^2$ at a dose rate of 1.5×10^{-4} dpa/s. (b) and (c) show SAED patterns acquired from two adjacent grains.

The curtaining contrast extending across the STEM image in Fig. 15(a) is an artifact introduced during FIB specimen preparation and should not be interpreted as a microstructural feature induced by He^+ or D_2^+ irradiation. The SAED patterns in Figs. 15(b) and 15(c), acquired from two adjacent grains, demonstrate that the grains have different crystallographic orientations. Unfortunately, the grain located in the top center of the image could not be brought into the desired orientation because its required tilt exceeded the available microscope tilt range. The adjacent grain on the right, however, was successfully aligned to the [101] zone axis. The absence of a continuous amorphous layer and large blisters at the lower dose rate is particularly noteworthy given that the total irradiation fluence and temperature are same as those used in the higher-dose-rate experiments. This observation provides further evidence that dose rate plays a critical role in determining whether irradiation-induced defects accumulate faster than they can recover. At the lower dose rate, more time for defect recombination and migration to sinks can prevent the accumulation of sufficient disorder to drive amorphization. Similarly, more effective relaxation of implanted-gas and vacancies may suppress the formation and growth of large He blisters.

The precipitate-cavity-containing layer observed beneath the crystalline surface is nevertheless indicative of substantial irradiation-induced chemical and defect evolution. The formation of these precipitates suggests that local Li redistribution and precipitation can still occur at the lower dose rate, even though the overall Li depletion measured by ToF-SIMS is limited. The cavities associated with the precipitates further indicate that vacancy clustering remains active under these conditions. At the lower dose rate, defect recovery limits the accumulation and growth of irradiation-induced features, whereas at the higher dose rate, rapid defect production overwhelms recovery and produces extensive Li redistribution, blister formation, and cavity growth.

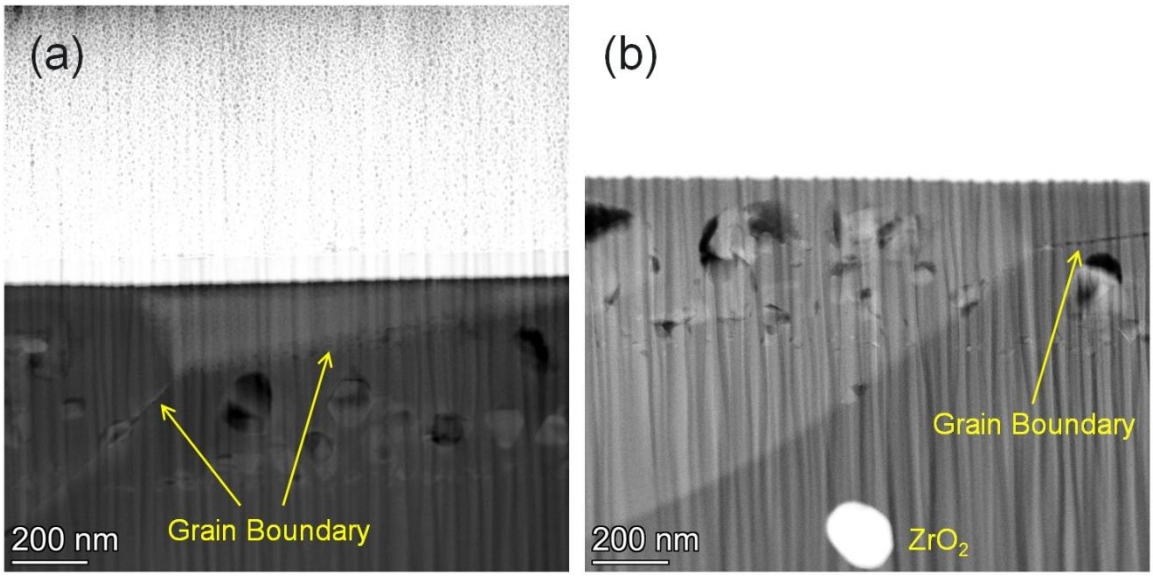


Figure 16. STEM micrographs showing two grain-boundary regions in a γ-$LiAlO_2$ pellet irradiated to 2×10^{17} $(He^+ + D^+)/cm^2$ at 773 K at a dose rate of 1.5×10^{-4} dpa/s.

Grain-boundary effects are also evident in the low-dose-rate sequentially irradiated specimen. As shown in Fig. 16, portions of grain boundaries lie within the irradiated region. In multiple locations, cavities are preferentially concentrated along the grain boundaries, indicating that these interfaces act as efficient sinks for irradiation-induced point defects and implanted gas species. Enhanced transport along grain boundaries can facilitate the migration and accumulation of vacancies, He, and D, thereby promoting cavity nucleation and growth at the interfaces. The preferential grain-boundary cavity formation observed at the lower dose rate is consistent with the corresponding behavior identified under D_2^+-only irradiation and suggests that grain boundaries can remain important microstructural sinks even when bulk defect accumulation is reduced. The apparent grain-boundary preference for cavity formation also highlights the role of local microstructure in determining the final irradiation response. Even under nominally identical irradiation conditions, the local cavity density and precipitate morphology can vary substantially depending on grain orientation, boundary character, and proximity to other sinks. These microstructural variations may contribute to the heterogeneous D retention and Li redistribution.

Overall, comparison of the low- and high-dose-rate experiments demonstrates a strong dose-rate dependence of both chemical and microstructural evolution in γ-$LiAlO_2$ at 773 K. Prior He^+ irradiation

consistently enhances subsequent non-gas D retention, attributed to He-vacancy clusters as D trapping sites. Lowering the dose rate further increases the apparent non-gas D retention while substantially suppressing Li depletion and large-scale blister formation. At the same time, precipitate formation and cavity nucleation remain evident, particularly near grain boundaries. These observations indicate that the irradiation response is governed by the competition between radiation-induced defect production and irradiation-enhanced, thermally activated recovery, diffusion, and defect-sink processes. Further STEM characterization of the individual He^+-only and D_2^+-only irradiated regions is still needed to clarify the contributions of He^+ irradiation and D^+ implantation to the observed precipitation and cavity evolution.

4. Conclusions

A systematic investigation was conducted to elucidate the individual and combined effects of He^+ and D_2^+ irradiation on the microstructural evolution, deuterium retention, and Li redistribution in γ-$LiAlO_2$ pellets. Individual and sequential 120 keV He^+ and 80 keV D_2^+ irradiations were performed using masks to create three distinct regions on the same pellet: He^+-only, D_2^+-only, and sequential He^+ and D_2^+. SRIM13 simulations were used to select irradiation conditions that produced overlapping He^+-induced damage and implanted D profiles. Two γ-$LiAlO_2$ pellets were irradiated at 773 K to 2×10^{17} He^+/cm^2, 2×10^{17} D^+/cm^2, and 2×10^{17} $(He^+ + D^+)/cm^2$ in three regions at two ion fluxes of ~4×10^{12} and ~1×10^{13} $(ions/cm^2)/s$, corresponding to combined dose rates of ~1.5×10^{-4} and ~3.8×10^{-4} dpa/s, respectively. The main conclusions are summarized as follows:

1. ToF-SIMS measurements show higher non-gas D retention when D_2^+ irradiation is preceded by He^+ irradiation than under D_2^+-only irradiation. The overall non-gas D retention at the low dose rate is higher than at the higher dose rate. This behavior is consistent with greater time for D diffusion and trapping at stable He-vacancy clusters. The broad, non-Gaussian D profiles indicate thermally activated D diffusion followed by trapping at irradiation-induced defects. The enhanced retention is attributed primarily to the formation of stable He-vacancy clusters that provide trapping sites.

2. At the higher dose rate, substantial Li depletion occurs under all irradiation conditions, with the greatest depletion following sequential He^+ and D_2^+ irradiation. Nearly complete Li depletion extends ~300 nm from the surface in the sequentially irradiated region. In contrast, Li depletion is strongly suppressed at the low dose rate, indicating that dynamic recovery and defect recombination limit radiation-enhanced Li transport.

3. He^+ irradiation at the higher dose rate produces He blisters, an ~170-nm-thick polycrystalline, Li-depleted layer containing precipitates and nanoscale cavities, an ~90-nm-thick lattice-strained transition region, and, tentatively, a deeper, featureless crystalline matrix in which non-gas D remains trapped. Cavities are uniformly distributed within the polycrystalline layer, with no clear evidence of preferential accumulation along grain boundaries. In contrast, D_2^+-only irradiation preserves an ~160-nm-thick monocrystalline surface layer and produces an underlying ~160-nm-thick region containing large, faceted $LiAl_5O_8$-type precipitates surrounded by cavities, with preferential cavity formation along grain boundaries.

4. At 773 K, thermally activated and irradiation-enhanced Li transport produces locally Li-deficient regions that favor formation of non-stoichiometric $LiAl_5O_8$-type precipitates. A strong spatial association is observed between the precipitates and surrounding cavities. The evolution from poorly defined

precipitates accompanied by small cavities to well-faceted precipitates surrounded by larger cavities suggests a coupled process involving Li redistribution, nucleation and growth of Li-deficient regions, and vacancy clustering and coarsening, rather than independent formation of precipitates and cavities.

5. Sequential He^+ and D_2^+ irradiation at the higher dose rate produces a completely amorphized surface layer of ~280 nm in thickness, followed by a region containing precipitates and associated cavities. The amorphous layer results from subsequent D_2^+ irradiation of the polycrystalline and lattice-strained regions generated by prior He^+ irradiation, whereas the deeper precipitate-cavity region develops from D_2^+ irradiation of the initially featureless crystalline region containing trapped non-gas D.

6. Unlike the high-dose-rate condition, sequential He^+ and D_2^+ irradiation at the low dose rate produces neither an amorphous surface layer nor large He blisters. A crystalline surface layer is retained, followed by a precipitate-cavity-containing region, with preferential cavity formation at grain boundaries.

Overall, the irradiation response of γ-$LiAlO_2$ at elevated temperature is governed by the coupled effects of displacement damage, He-vacancy clustering, D transport and trapping, Li redistribution, precipitation, cavity evolution, and microstructural sinks. These findings provide a mechanistic basis for understanding tritium trapping and microstructural evolution in γ-$LiAlO_2$ under neutron irradiation.

5. Acknowledgments

This work was supported by Tritium Modernization Program, sponsored by National Nuclear Security Administration (NNSA), U.S. Department of Energy (DOE).

6. References

[1] W. Jiang *et al*., J. Nucl. Mater. 511 (2018) 1.
[2] W. Jiang *et al*., J. Nucl. Mater. 591 (2024) 154925.
[3] W. Jiang *et al*., J. Nucl. Mater. 538 (2020) 152357.
[4] W. Jiang *et al*., J. Nucl. Mater. 494 (2017) 411.
[5] W. Jiang, A.M. Casella, D.J. Senor, *Effects of irradiation temperature on the microstructure and deuterium retention in γ-$LiAlO_2$ pellets*, PNNL-36560, September 2024.
[6] W. Jiang, A.M. Casella, D.J. Senor, *Effects of dose rate on the microstructure and deuterium retention in γ-$LiAlO_2$ pellets*, PNNL-38365, September 2025.
[7] W. Jiang *et al*., J. Appl. Phys. 139 (2026) 155902.
[8] J.F. Ziegler, J.P. Biearsack, U. Littmark, *The stopping and Range of Ions in Solids* (Pergamon Press, New York, 1985); available at: http://www.SRIM.org/.
[9] W. Jiang, *et al*., J. Nucl. Mater. 542 (2020) 152532.
[10] H. Tsuchihira, T. Oda, and S. Tanaka, Nucl. Instr. Meth. Phys. Res. B 269 (2011) 1707.
[11] Y. Zhou, M. Xia, V. Suseela, H.M. Kao, R.M. Asmussen, A. Bhattacharjee, C.A. Creamer, M. Liu, J.G. Wang, Z. Zhu, Anal. Chem. 97 (2025) 8755.
[12] W. Jiang *et al*., J. Nucl. Mater. 484 (2017) 374.
[13] W. Jiang *et al*., J. Appl. Phys. 131 (2022) 215902.
[14] W. Jiang *et al*., Ceram. Int. (2026) in press, https://doi.org/10.1016/j.ceramint.2026.05.174.